applied sciences

MDPI

Article

Image-Based Fourier Reconstruction and Analysis of Free-Surface Wave Motion in a CNC-Excited Rectangular Reservoir

Elsagir Almaksoudi [1,*], Miloš Nedeljković [1], Dejan B. Ilić [1], Rawasy Almaksoudi [2] and Omar Bećiragić [1]

[1] Faculty of Mechanical Engineering, University of Belgrade, Kraljice Marije 16, 11120 Belgrade, Serbia; mnedeljkovic@mas.bg.ac.rs (M.N.); dilic@mas.bg.ac.rs (D.B.I.); omarbeciragic@gmail.com (O.B.)

[2] Department of Engineering, Swarthmore College, 500 College Avenue, Swarthmore, PA 19081, USA; rawasycat@gmail.com

* Correspondence: melsagir@gmail.com

Abstract

Free-surface sloshing in partially filled tanks and open reservoirs can produce spatially complex surface deformation under horizontal excitation. This study presents an image-based experimental and computational workflow for reconstructing measured free-surface profiles in a laboratory-scale rectangular reservoir mounted on a Haas VF-3/VF-3SS-family CNC machining center. The tank underwent a programmed horizontal back-and-forth motion. The retained CNC controller record shows commanded x positions spanning approximately -19.976 mm to $+19.851$ mm, corresponding to a programmed peak-to-peak stroke of approximately 39.8 mm. The realized forcing frequency was not independently measured; therefore, no experimental near-resonance condition is claimed. Videos were recorded approximately normal to the transparent tank wall, converted to still frames, calibrated directly in physical length units, and manually digitized with WebPlotDigitizer. A truncated spatial Fourier series was fitted independently to each measured time slice. The accompanying Python applications dynamically evaluate the experimentally fitted representation: the GUI tools animate reconstructed profiles over the recorded time sequence, while the final FourierN3 implementation builds time-dependent coefficient models, linearly interpolates coefficient histories, evaluates $y(x,t)$, and generates a three-dimensional space–time reconstructed surface. These outputs are described as dynamic Fourier reconstructions because they remain conditioned on measured coefficient histories and do not constitute independent CFD or potential-flow predictions. The Fourier harmonics are mathematical reconstruction functions and are not identified one-to-one with physical sloshing eigenmodes. For a 0.45 m tank length, linear theory gives first-mode reference frequencies of 0.687 Hz at a 4 cm water depth and 0.763 Hz at a 5 cm water depth. The workflow is demonstrated on three selected datasets that provided sufficiently clear free-surface records for consistent frame-by-frame digitization. Using a common three-harmonic benchmark, mean RMSE values were 0.8815 cm for Case A (4 cm), 1.419 cm for Case B (5 cm), and 0.5022 cm for Case C (4 cm), corresponding to mean NRMSE values of 22.0%, 28.4%, and 12.6%, respectively. For Case C, adding a fourth harmonic reduced the mean RMSE to 0.4427 cm (11.1% of water depth), an 11.8% reduction relative to the three-harmonic fit. All RMSE and NRMSE values are reconstruction errors relative to the manually digitized coordinates, not estimates of absolute experimental measurement accuracy. The results therefore demonstrate the reconstruction workflow for the three selected records rather than establish a general water-depth effect.

Received: 20 July 2026
Revised: 6 September 2026
Accepted: 8 September 2026
Published: 9 September 2026

 https://doi.org/10.3390/app16188956

Keywords: free-surface sloshing; image-based measurement; Fourier reconstruction; dynamic reconstruction; rectangular reservoir; WebPlotDigitizer; CNC excitation; RMSE; NRMSE; reduced-order representation

1. Introduction

Free-surface sloshing in partially filled tanks and open reservoirs is relevant to hydraulic machinery, pumped-storage systems, liquid-storage vessels, marine structures, and other engineering systems in which container motion can generate transient surface deformation and unsteady loads. Classical sloshing theory shows that response depends on tank geometry, fill depth, excitation frequency and amplitude, damping, and internal structures such as baffles [1–7]. Recent experiments continue to document nonlinear response, depth-dependent behavior, phase effects, and higher-harmonic content in rectangular tanks [8–11].

Measurement technology has developed in parallel with the underlying sloshing theory. Image-based methods are attractive because they can recover the spatial free-surface shape rather than only a single-point elevation or pressure signal. Tosun et al. used image processing to track the free surface and estimate sloshing force, while Liu et al. combined image processing with a hydrodynamic reconstruction framework [12,13]. More recent work has used artificial intelligence segmentation to identify the free surface in sloshing tanks [14], machine learning frameworks to characterize nonlinear sloshing dynamics [15], stereo-vision profilometry to obtain dense water-surface profiles [16], and image-based deep learning to infer sloshing pressure from wave images [17]. These developments show a progression from manual or rule-based image extraction toward increasingly automated and data-driven measurement and interpretation.

High-fidelity numerical methods, including finite-volume, volume-of-fluid, finite-element, arbitrary Lagrangian–Eulerian, and meshless approaches, can resolve detailed flow fields and pressure loads [18–20]. Such methods are essential when the objective is predictive fluid dynamics, but they require well-defined forcing histories and boundary conditions. Experimental studies also benefit from lower-order representations that convert recorded surface shapes into compact descriptors without claiming to replace a governing-equation solver.

The present study addresses this experimental-data problem. A transparent rectangular tank was mounted on a Haas VF-3/VF-3SS-family CNC machining center and translated horizontally to generate free-surface waves. Video frames were calibrated and manually digitized with WebPlotDigitizer (Automeris; https://automeris.io; accessed on 5 June 2026) [21], and each measured spatial profile was independently reconstructed with a truncated Fourier series. The resulting coefficient, amplitude, residual, and error histories provide a compact description of the observed surface geometry. Python graphical applications then evaluate the fitted representation dynamically: reconstructed profiles can be animated through time, and the final FourierN3 implementation constructs time-dependent coefficient models and a three-dimensional x–t–y reconstructed surface.

The novelty of the work is therefore not the Fourier series itself. Rather, the contribution is the integration of (i) a CNC machining platform used as a controllable horizontal excitation device, (ii) image-derived centimeter-calibrated free-surface coordinates, (iii) time-slice spatial Fourier reconstruction, (iv) dynamic evaluation and visualization of the fitted $y(x,t)$ representation, and (v) residual, normalized-error, and harmonic-order diagnostics in a reproducible analysis workflow. In contrast with a temporal spectrum that primarily identifies frequencies in a signal, the present procedure reconstructs the full measured spatial profile at each selected time. The dynamic Python output is described throughout this manuscript as an animated and interpolated reduced-order reconstruction of the measured data. It is not an independent physics-based prediction because its coefficient histories originate from the measured profiles rather than from a solution of the governing fluid equations.

The manuscript also distinguishes two mathematical objects that should not be conflated: the wave numbers associated with linear physical sloshing modes and the periodic Fourier basis used solely to approximate the measured spatial profile. This distinction is important when interpreting the coefficient histories. The fitted harmonics are treated as geometric reconstruction components, not as one-to-one measurements of the tank's physical eigenmodes.

The remainder of the paper presents the theoretical reference frequencies, reconstruction equations, experimental setup, image-processing procedure, quantitative results for three selected datasets, uncertainty and harmonic-order considerations, and the limits of physical interpretation supported by the retained experimental record.

2. Materials and Methods

2.1. Linear Sloshing Frequency as a Theoretical Reference

For small-amplitude inviscid sloshing in a rectangular tank, the natural angular frequency may be expressed as

$$\omega_n^2 = g k_n \tanh(k_n h), \quad (1)$$

where ω_n is the angular frequency of mode n, g is gravitational acceleration, h is the water depth, and k_n is the corresponding physical sloshing wave number. For the mode family used in the experimental notes,

$$k_n = \frac{(2n-1)\pi}{L_t}, \quad (2)$$

where L_t is the tank length in the excitation direction. For the first mode ($n = 1$) and $L_t = 0.45$ m,

$$k_1 = \frac{\pi}{0.45} = 6.981 \text{ m}^{-1}. \quad (3)$$

Using $g = 9.81$ m/s^2 gives the theoretical reference values in Table 1.

Table 1. First-mode linear sloshing reference frequencies for the two analyzed nominal water depths. These values are theoretical references; the experimental CNC forcing frequency was not independently recorded.

Water Depth h	k_1 (m^{-1})	ω_1 (Rad/s)	f_1 (Hz)
0.04 m	6.981	4.318	0.687
0.05 m	6.981	4.794	0.763

The experimental protocol used the estimated first-mode natural frequency as a design reference. The programmed displacement range is documented by the retained CNC controller record (Section 2.5.1), but a synchronized measurement of the realized table displacement $x(t)$ and forcing period was not acquired. Accordingly, the values in Table 1 are used only as theoretical references: no numerical forcing ratio such as ω/ω_0 is reported, and no experimentally verified near-resonance condition is claimed.

2.2. Fourier Reconstruction Basis and Its Relation to Physical Modes

At a selected time t, the measured free-surface profile is represented by spatial coordinates $y(x,t)$. The profile is reconstructed using a truncated Fourier series over the measured profile domain,

$$y_{\text{fit}}(x,t) = a_0(t) + \sum_{m=1}^{N}\left[a_m(t)\cos\left(\frac{2\pi m(x-x_0)}{L_p}\right) + b_m(t)\sin\left(\frac{2\pi m(x-x_0)}{L_p}\right)\right], \quad (4)$$

where x_0 is the first measured horizontal coordinate, L_p is the measured profile span for that time slice, N is the reconstruction order, and $a_m(t)$ and $b_m(t)$ are fitted coefficients.

Equation (4) is a mathematical fitting basis. Its periodic spatial wave numbers, $2\pi m/L_p$, are not assumed to equal the physical sloshing wave numbers k_n in Equation (2). The physical-mode relation is used only for the theoretical natural-frequency reference calculation, whereas the Fourier basis is used to approximate the geometry of each digitized surface profile. Consequently, references to the fitted terms as physical sloshing modes have been avoided. They are described below as spatial Fourier harmonics or reconstruction components.

For the common $N = 3$ reconstruction, the implementation is

$$\begin{aligned} y_{\text{fit}}(x,t) = c_0(t) + c_1(t)\cos\theta + c_2(t)\sin\theta + c_3(t)\cos(2\theta) + c_4(t)\sin(2\theta) \\ + c_5(t)\cos(3\theta) + c_6(t)\sin(3\theta), \end{aligned} \quad (5)$$

with

$$\theta = \frac{2\pi(x-x_0)}{L_p}. \quad (6)$$

For Case C, an $N = 4$ fit was also available and adds $c_7(t)\cos(4\theta) + c_8(t)\sin(4\theta)$.

2.3. Harmonic Amplitudes and Phases

For the common $N = 3$ representation, the amplitudes of the three spatial Fourier components are

$$A_1 = \sqrt{c_1^2 + c_2^2}, \qquad A_2 = \sqrt{c_3^2 + c_4^2}, \qquad A_3 = \sqrt{c_5^2 + c_6^2}, \quad (7)$$

and the associated phases are

$$\phi_1 = \text{atan2}(c_2, c_1), \qquad \phi_2 = \text{atan2}(c_4, c_3), \qquad \phi_3 = \text{atan2}(c_6, c_5). \quad (8)$$

The coefficient $c_0(t)$ describes the vertical offset or mean level of the fitted profile. The first coefficient pair describes the broadest periodic component available in the chosen Fourier basis; subsequent pairs describe progressively shorter spatial scales. Their amplitudes and phases are therefore useful geometric descriptors of changing waveform shape, but they are not interpreted as direct measurements of the physical eigenmode amplitudes of the tank.

2.4. Residual, RMSE, and Normalized RMSE

At a measured spatial point x_j,

$$r_j(t) = y_{\text{meas}}(x_j,t) - y_{\text{fit}}(x_j,t). \quad (9)$$

For a time slice containing M_t digitized points,

$$\mathrm{RMSE}(t) = \sqrt{\frac{1}{M_t}\sum_{j=1}^{M_t} r_j^2(t)}. \tag{10}$$

Because the coordinates were calibrated in centimeters in WebPlotDigitizer, RMSE is reported in centimeters. To provide a depth-relative benchmark, the normalized RMSE is also reported as

$$\mathrm{NRMSE}(t) = \frac{\mathrm{RMSE}(t)}{h}, \tag{11}$$

where h is the nominal water depth expressed in the same length unit.

Two distinct uncertainty concepts are important. RMSE quantifies disagreement between the Fourier reconstruction and the digitized coordinate set. It does not, by itself, quantify the absolute uncertainty of the physical free-surface location. The latter additionally depends on image calibration, boundary visibility, reflections, meniscus effects, perspective, blur, and manual point selection. This distinction is retained throughout Sections 3 and 4.

2.5. Experimental Setup

2.5.1. CNC Excitation Platform

A Haas VF-3/VF-3SS-family vertical machining center (Haas Automation, Inc., Oxnard, CA, USA) was repurposed as a horizontal excitation platform. The transparent tank was fixed to the CNC table, and table motion in the x-direction generated free-surface waves. Manufacturer documentation identifies the VF-3/VF-3SS family as three-axis vertical mills with a travel envelope sufficient for the laboratory arrangement [22,23].

The excitation was implemented through a programmed sequence of G01 linear moves along the CNC x-axis. The retained controller record shows commanded positions spanning approximately $x = -19.976$ mm to $x = +19.851$ mm, corresponding to a programmed peak-to-peak stroke of approximately 39.8 mm. The controller program also contains segment-specific feed commands during the reciprocating motion. The original experimental notes report a nominal feed setting of approximately 17.5 m/min (0.2917 m/s); this value is retained as an operating setting rather than interpreted as a complete time-resolved velocity history. A synchronized independent measurement of the realized table displacement $x(t)$, acceleration, reversal timing, and forcing period was not acquired. Consequently, the programmed stroke is documented, but no measured excitation frequency or resonance ratio is inferred retrospectively, and the excitation is not modeled as an ideal sinusoidal forcing function.

2.5.2. Tank Geometry and Instrumentation

The transparent rectangular reservoir had an approximate length and width of 450 mm and a total height of approximately 470 mm, with a wall thickness of about 5 mm. The measured free-surface profiles spanned approximately 45 cm in the excitation direction. The apparatus also contained pressure transducers from the broader experimental setup; their manufacturer and model were not retained in the analysis record. Pressure signals were not analyzed in the present study; the transducers are therefore documented only as part of the apparatus and are not used for validation or interpretation.

2.5.3. Experimental Run Matrix and Selection of Analyzed Cases

Eleven laboratory runs were documented at nominal water levels from 4 cm to 7.5 cm and excitation durations from 9 s to 17 s (Table 2). The present Fourier analysis does not claim to represent all eleven conditions. Three runs were selected because they provided the clearest and most usable free-surface records for complete frame-by-frame digitization and consistent Fourier reconstruction. These cases are therefore treated as a focused demonstration of the workflow rather than as a statistically complete study of water-depth effects.

The experimental setup and tank geometry are shown in Figures 1 and 2, respectively.

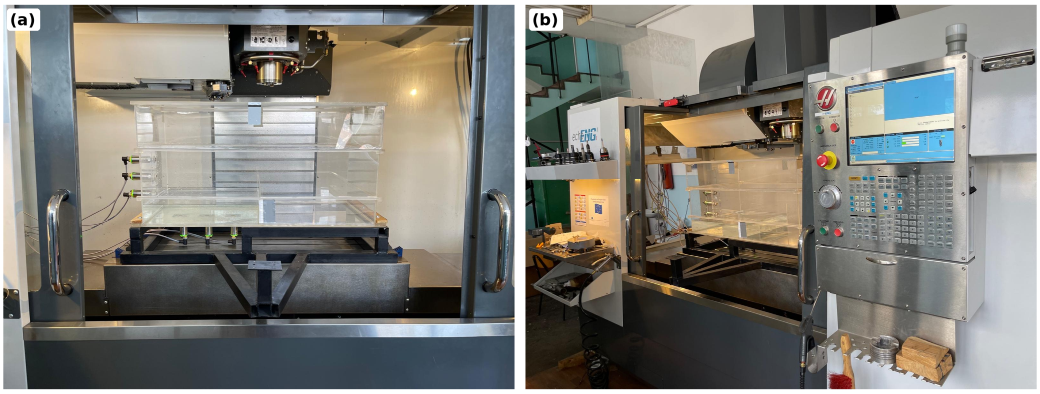

Figure 1. Experimental setup. (**a**) Transparent rectangular reservoir mounted on the CNC table inside the machining workspace. (**b**) Overall HAAS CNC installation and controller. The reservoir was excited by repeated horizontal table motion in the x-direction.

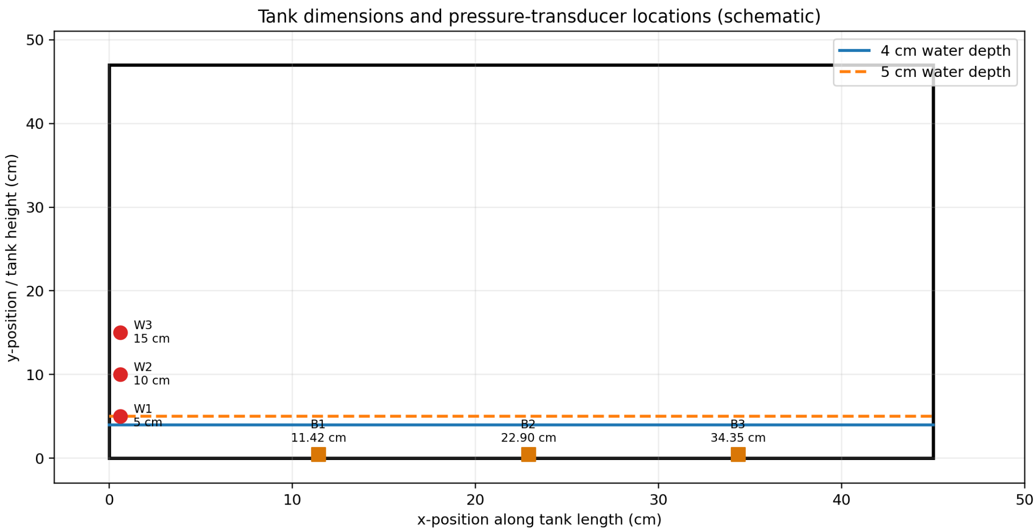

Figure 2. Schematic tank geometry used to document the approximately 45 cm profile span and the nominal 4 cm and 5 cm analyzed water depths. Pressure-transducer locations are shown only as apparatus documentation; pressure data are outside the scope of the present analysis.

Table 2. Experimental run matrix from the laboratory record. Three runs with the clearest usable free-surface records were selected for the detailed Fourier reconstruction presented in this study.

Run Index	Experiment Number	Water Level	Excitation Time
1	2951	7 cm	12 s
2	2952	7.5 cm	10 s
3	2953	5 cm	16 s
4	2955	5 cm	15 s
5	2958	4 cm	17 s
6	2959	4 cm	15 s
7	2960	4 cm	10 s
8	2961	4 cm	10 s
9	2962	4 cm	10 s
10	2963	4 cm	9 s
11	2964	4 cm	10 s

2.6. Image Acquisition, Calibration, and Digitization

The free surface was recorded from the transparent side wall with the camera positioned approximately straight-on to the tank. The raw videos were retained by the authors. Complete camera metadata (manufacturer/model, lens, exposure settings, original frame-rate metadata, and camera-to-tank distance) were not preserved in the experimental notes used for this analysis and are therefore not reconstructed retrospectively.

Spatial scale was established during digitization rather than inferred from camera specifications. In WebPlotDigitizer, each selected image was calibrated against known physical dimensions so that extracted coordinates were expressed directly in centimeters. The camera model and manufacturer were not preserved in the retained experimental record and therefore cannot be reported retrospectively. The camera model is not a numerical input to the Fourier fit; however, image resolution, viewing geometry, blur, optical distortion, reflection, transparency, and meniscus visibility can affect the precision with which the operator identifies the free-surface boundary and remain sources of measurement uncertainty.

Selected frames were manually digitized along the visible air–water interface. The number of digitized points M_t was not forced to be identical in every frame; more points could be used where local curvature or visibility required them. Across the three analyzed datasets, the total point counts and time slices imply approximately 19.8, 20.6, and 27.5 points per analyzed time slice for Cases A, B, and C, respectively. The red markers in Figure 3 show a representative extraction.

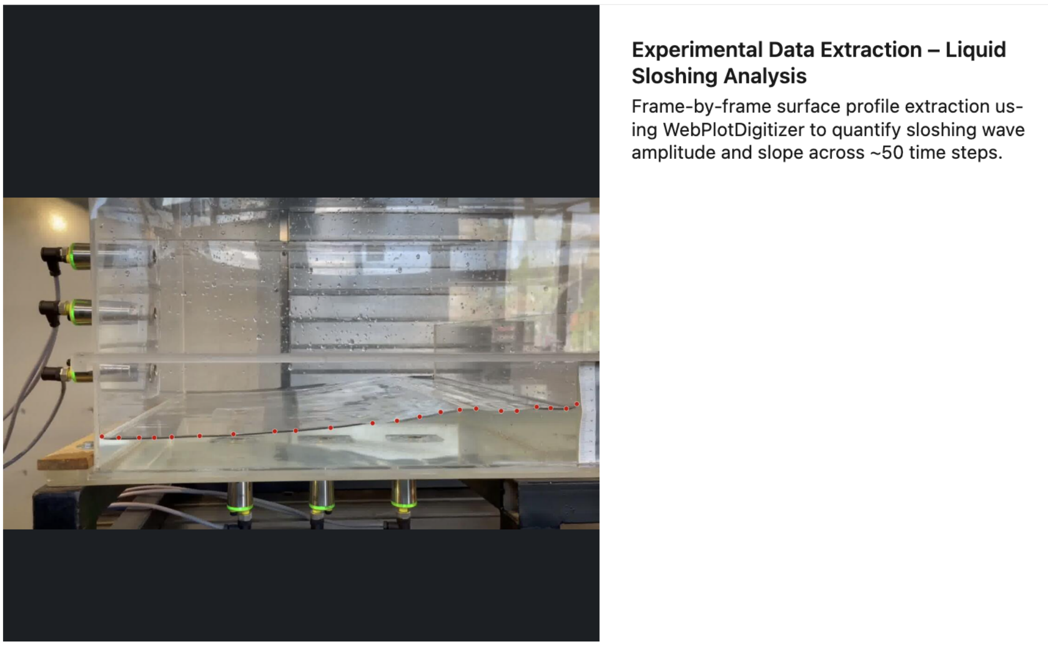

Figure 3. Representative frame-by-frame extraction of the visible free-surface boundary with WebPlotDigitizer. The red points illustrate the manually selected coordinates after calibration to physical length units.

A formal repeated-digitization or inter-operator study was not part of the original experimental campaign. Consequently, no unsupported pixel-level or operator-repeatability uncertainty is assigned. The reported reconstruction errors should be interpreted relative to the digitized profile, and this limitation is addressed explicitly in Section 4.6.

2.7. Software Workflow and Data Flow

Each processed data table contains $\{t, x, y\}$, where t is the selected frame time and (x, y) are the calibrated surface coordinates. The computational workflow was as follows:

1. Record CNC-driven free-surface motion;
2. Select still frames and assign time values;
3. Calibrate the image in centimeters in WebPlotDigitizer;
4. Manually trace the visible free-surface boundary;
5. Export $\{t, x, y\}$ coordinates;
6. Group points by time slice;
7. Fit Equation (4) by least-squares reconstruction for the selected harmonic order;
8. Calculate coefficient pairs, harmonic amplitudes, and phases;
9. Reconstruct y_{fit}, residuals, RMSE, and NRMSE;
10. Compare reconstruction error as harmonic order N is increased;
11. Evaluate the fitted time-dependent representation dynamically through profile animation and, in the final FourierN3 implementation, time interpolation of coefficient histories and a three-dimensional x–t–y Fourier surface.

The complete experimental-to-computational sequence is summarized in Figure 4.

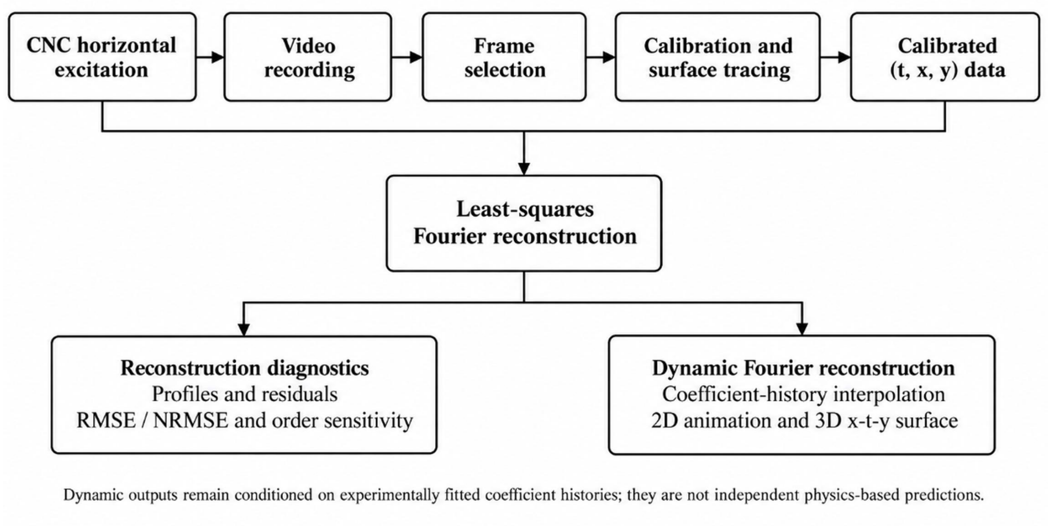

Figure 4. Experimental-to-computational workflow. Video frames were calibrated and digitized in WebPlotDigitizer, exported as t, x, y data, grouped by time, and fitted with the Fourier software. The workflow produces reconstruction diagnostics and a dynamic Fourier reconstruction. In the final FourierN3 implementation, fitted coefficient histories can be interpolated to evaluate $y(x, t)$, animate reconstructed 2D profiles, and form a 3D space–time reconstructed surface.

2.8. Dynamic Fourier Reconstruction and Software Implementation

The computational tools do more than generate static coefficient plots. The analyses and graphical applications were run in Python 3.13 (Python Software Foundation; https://www.python.org/). The `wave_gui_app2` and `setup` Python GUIs read measured t, x, y data, group the rows by time, build the sine–cosine design matrix, and obtain the Fourier coefficients by linear least squares. The applications then evaluate the fitted profile and provide interactive time selection together with Play, Pause, and Reset controls for animation of the reconstructed free surface over the recorded time sequence.

The final `FourierN3` implementation extends this idea into a time-dependent reduced-order reconstruction. Its program structure includes routines for building coefficient models in time, linearly interpolating the fitted coefficient histories, evaluating reconstructed height at a selected (x, t), animating the 2D reconstructed profile, and forming a 3D reconstructed Fourier surface without superimposed experimental points. Because the coefficient histories are obtained from measured surface profiles, these outputs are described as dynamic or interpolated reconstructions. They do not provide an independent prediction for a new forcing condition and are not presented as CFD, a Navier–Stokes solution, or independent physical validation.

For clarity, descriptive case names are used throughout the Results. The original file/software identifiers are retained only in Table 3 to preserve traceability.

Table 3. Case nomenclature, internal analysis identifiers, and software role.

Case	Depth	Internal Analysis Identifier	Software Role
A	4 cm	`wave_gui_app2` `WLEX`	Three-harmonic least-squares spatial fit at each recorded time, interactive evaluation, and profile animation.
B	5 cm	`setup` `WLPY_5cm_N4`	Flexible data-loading GUI using the measured height column; common $N = 3$ fit used for cross-case comparison, with interactive profile animation.
C	4 cm	`FourierN3` `WLEX_fourier_N4_values`	$N = 3/N = 4$ comparison and final time-dependent Fourier implementation, including coefficient interpolation, 2D reconstructed-profile animation, and 3D space–time reconstructed-surface visualization.

2.9. Choice of Harmonic Order

The common $N = 3$ model is a deliberately chosen low-order benchmark used so that Cases A, B, and C can be compared under the same reconstruction complexity; it is not presented as an objectively selected optimum. Harmonic-order sensitivity plots are used to show what is gained by increasing N. Case C provides a direct $N = 3$ versus $N = 4$ comparison. For Case B, the continuing decrease in error as additional harmonics are included indicates that three harmonics do not fully represent all spatial detail in that case. Formal automatic model-order selection by cross-validation, AIC, or BIC was not part of the original workflow and is therefore proposed as a future extension rather than invoked retrospectively.

2.10. Notation

The principal symbols used throughout the manuscript are summarized in Table 4.

Table 4. Principal notation used in the manuscript.

Symbol	Definition
x, y	Horizontal and vertical coordinates of the digitized free surface
t	Time associated with a selected frame/profile
h	Nominal water depth
L_t	Physical tank length in the excitation direction (0.45 m)
L_p	Measured spatial span of a digitized profile used in the Fourier fit
k_n	Physical sloshing wave number used in the linear natural-frequency relation
ω_n, f_n	Angular and cyclic natural frequencies of a theoretical sloshing mode
N	Number of spatial Fourier harmonics retained in the reconstruction
$c_0, \ldots, c_{2N}$	Time-dependent fitted Fourier coefficients
A_m, ϕ_m	Amplitude and phase of Fourier reconstruction harmonic m
M_t	Number of digitized spatial points in time slice t
RMSE	Root-mean-square difference between digitized and reconstructed profiles
NRMSE	RMSE normalized by nominal water depth, RMSE/h

3. Results

3.1. Dataset Summary and Depth-Normalized Error

Table 5 summarizes the three selected cases. The principal cross-case comparison uses the common $N = 3$ basis. The $N = 4$ Case C result is included to quantify the sensitivity to one additional harmonic. NRMSE provides a benchmark relative to the nominal water depth rather than treating a centimeter of error as equivalent across depths.

Table 5. Summary of the selected Fourier reconstruction cases. RMSE is fitting error relative to the digitized profiles, and NRMSE is the mean RMSE divided by nominal water depth.

Case	Depth	Model	Time Slices	Data Points	Mean RMSE (cm)	Max RMSE (cm)	Mean NRMSE
A	4 cm	$N = 3$	138	2727	0.8815	3.974	0.220 (22.0%)
B	5 cm	$N = 3$	144	2966	1.419	5.962	0.284 (28.4%)
C	4 cm	$N = 3$	100	2749	0.5022	3.581	0.126 (12.6%)
C	4 cm	$N = 4$	100	2749	0.4427	3.303	0.111 (11.1%)

The mean NRMSE values show that the reconstruction error is not negligible relative to the shallow water depths. The three-harmonic Case C reconstruction performs best of the common-order comparisons, whereas Case B has the largest mean depth-normalized reconstruction error. These values should not be interpreted as camera-measurement uncertainty; they quantify only the agreement between the fitted Fourier profile and the manually digitized points.

3.2. Case C: 4 cm Reconstruction and $N = 3$–$N = 4$ Sensitivity

Case C contains 100 time slices and 2749 digitized points. The $N = 3$ reconstruction has a mean RMSE of 0.5022 cm and a maximum RMSE of 3.581 cm. The time-resolved curve in Figure 5 shows that most intervals are reconstructed with substantially lower error than the largest transient spikes. The residual map (Figure 6) identifies where those disagreements occur in both time and position, while representative profile comparisons (Figure 7) show that the low-order fit follows the broad measured geometry and smooths some local irregularities.

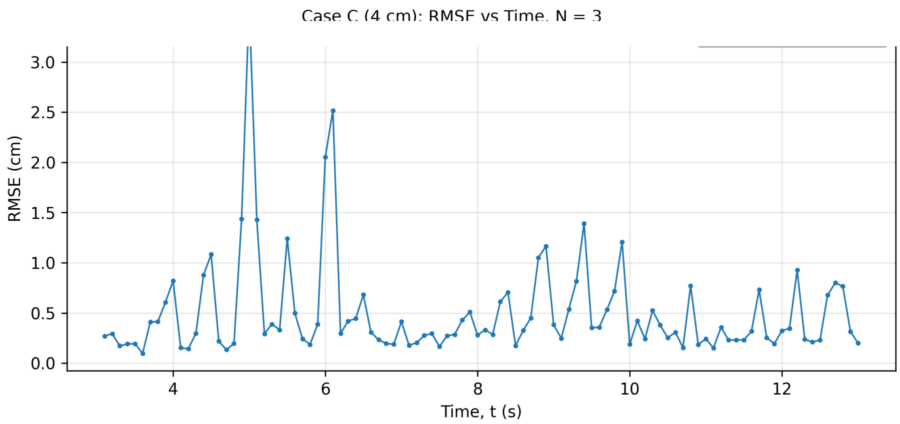

Figure 5. Case C (4 cm): RMSE versus time for the common $N = 3$ reconstruction. The mean RMSE is 0.5022 cm and the maximum is 3.581 cm. One transient value exceeds the displayed vertical plotting range; its numerical maximum is stated here and in the main text.

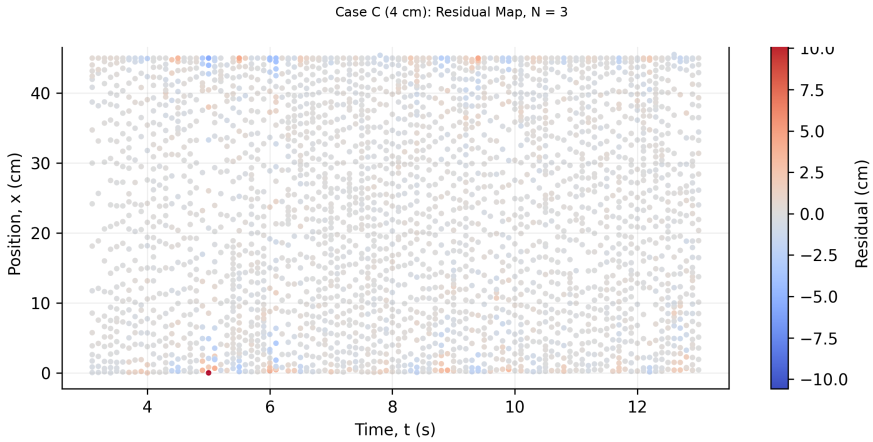

Figure 6. Case C (4 cm): residual map $y_{\mathrm{meas}} - y_{\mathrm{fit}}$ for the $N = 3$ reconstruction. Localized regions of larger residual identify time–position combinations that are not fully represented by the low-order fit.

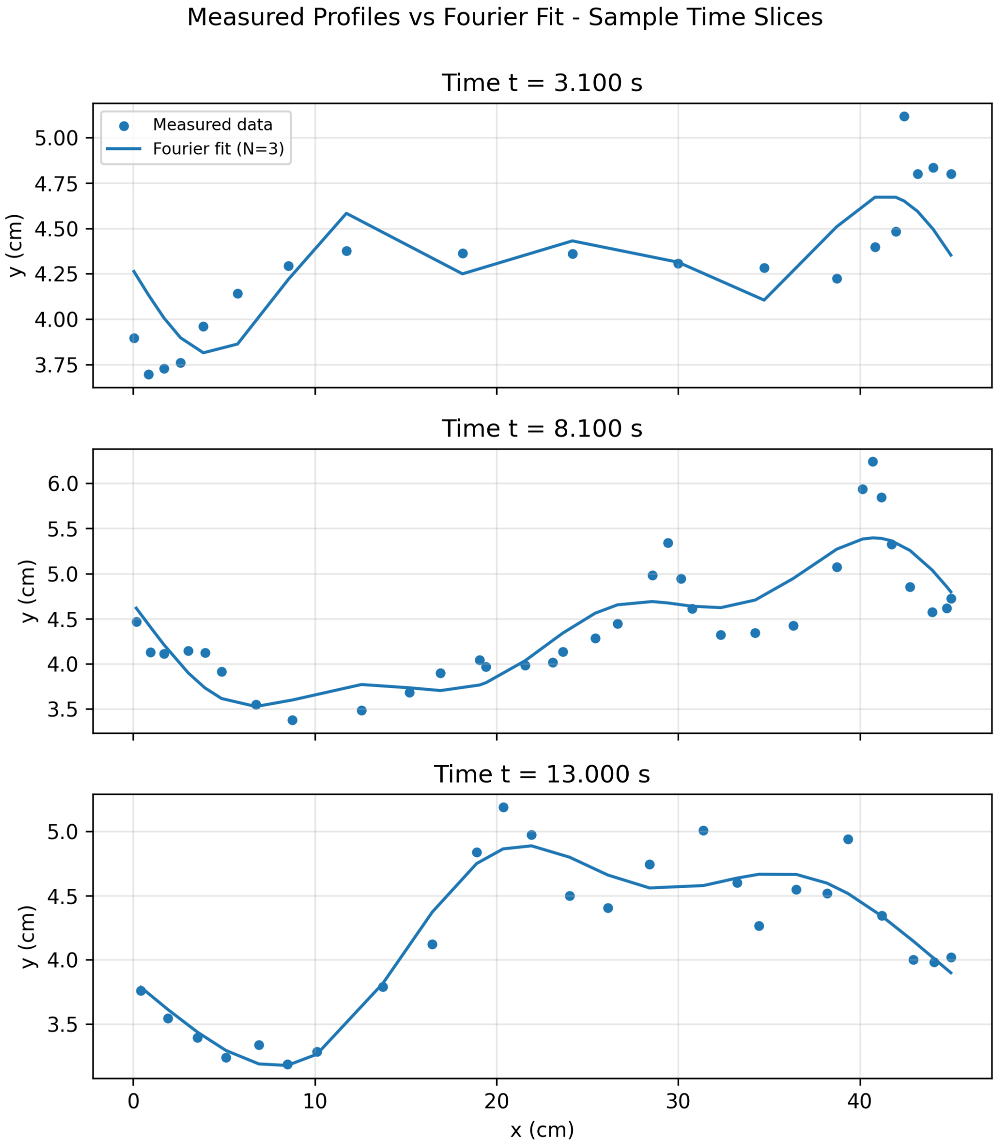

Figure 7. Case C (4 cm): representative measured profiles and $N = 3$ Fourier reconstructions. The low-order basis captures the broad surface geometry while smoothing local point-level variation.

Figure 8 shows the reduction in average error as the harmonic order increases. The available direct comparison gives 0.5022 cm for $N = 3$ and 0.4427 cm for $N = 4$. Thus, adding the fourth harmonic reduces the mean RMSE by approximately 11.8%. This is a measurable improvement, but it also demonstrates why $N = 3$ should be treated as a common comparison order rather than an optimal order selected by an objective information criterion.

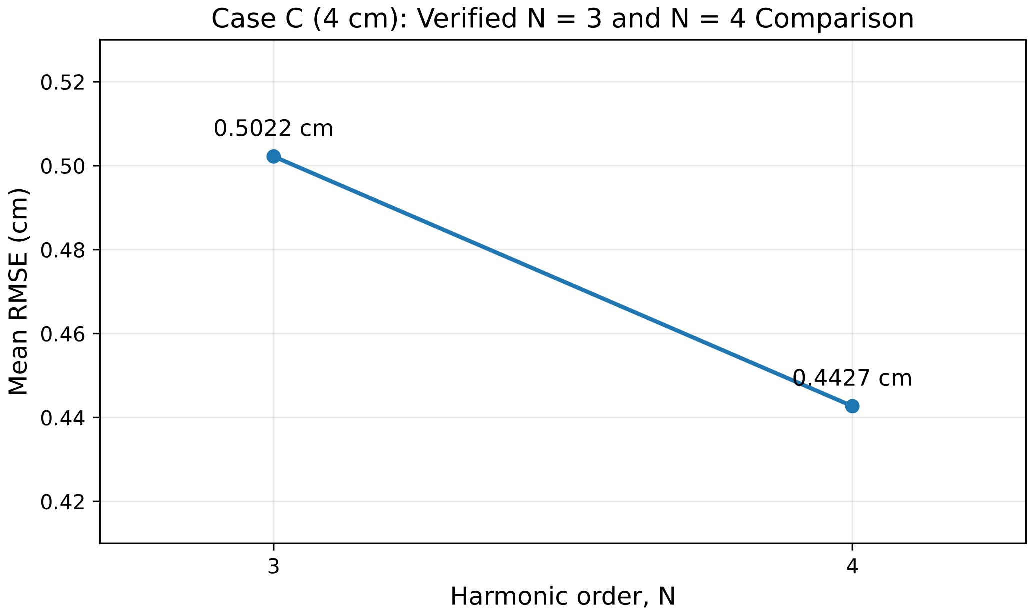

Figure 8. Case C (4 cm): verified direct comparison of mean RMSE for the $N = 3$ and $N = 4$ reconstructions. Both values use the same Case C dataset and the same time-slice averaging definition reported in Table 5.

3.3. Case A: 4 cm Coefficient Evolution and Reconstruction Error

Case A contains 138 time slices and 2727 digitized points. The fitted coefficient histories show that the profile offset and oscillatory coefficient pairs vary throughout the experiment as the measured spatial geometry changes. The $c_0(t)$ history tracks the profile offset, while the paired oscillatory coefficients define the three retained spatial reconstruction components. Their variation is interpreted as a compact description of the digitized waveform, not as a direct measurement of physical tank eigenmodes.

The corresponding amplitudes (Figure 9) show that the relative contributions of the three spatial components change throughout the experiment. A larger higher-order amplitude indicates that a shorter spatial scale contributes more strongly to the mathematical representation of that frame; it does not, by itself, identify a physical sloshing mode.

The mean RMSE is 0.8815 cm and the maximum RMSE is 3.974 cm, corresponding to a mean NRMSE of 22.0%. The error is strongly time-dependent (Figure 10), with intervals of relatively low disagreement interrupted by larger spikes. The harmonic-order sensitivity curve (Figure 11) confirms that additional terms reduce the fitting error, as expected for a nested Fourier representation. The time-resolved RMSE and harmonic-order sensitivity provide direct context for the reported mean fitting error.

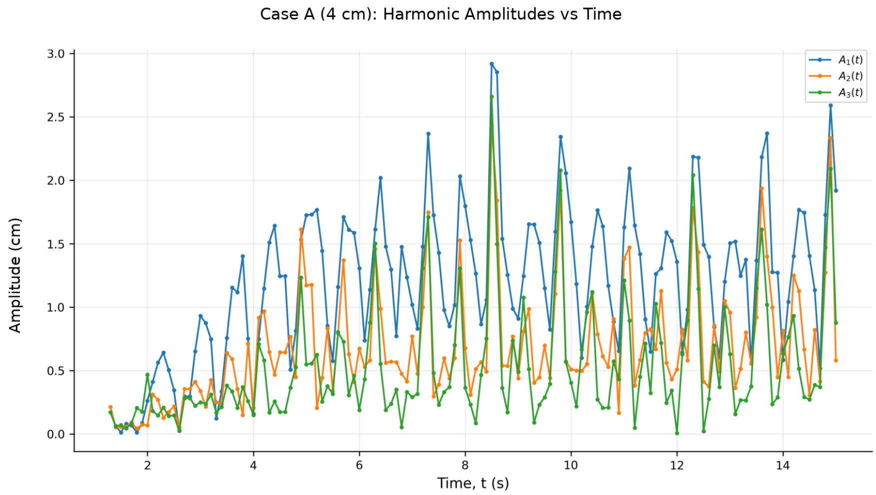

Figure 9. Case A (4 cm): amplitudes of the first three spatial Fourier reconstruction components versus time.

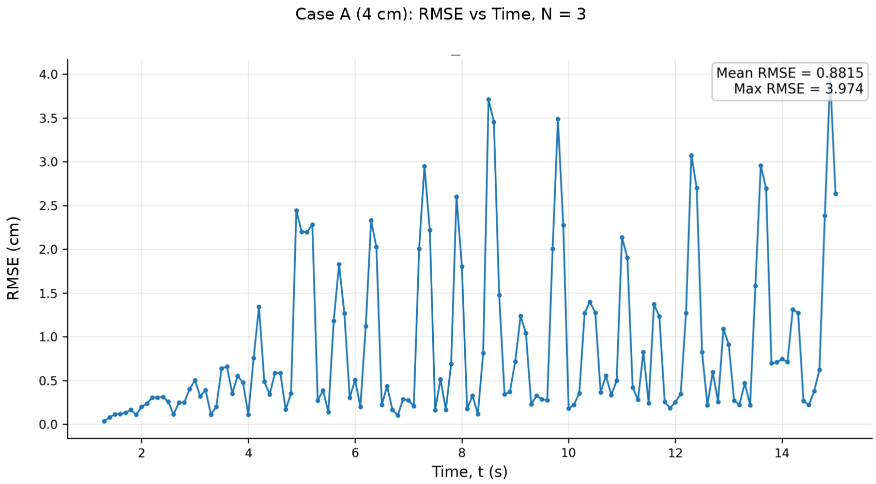

Figure 10. Case A (4 cm): RMSE versus time for the common $N = 3$ reconstruction. Mean RMSE is 0.8815 cm and maximum RMSE is 3.974 cm.

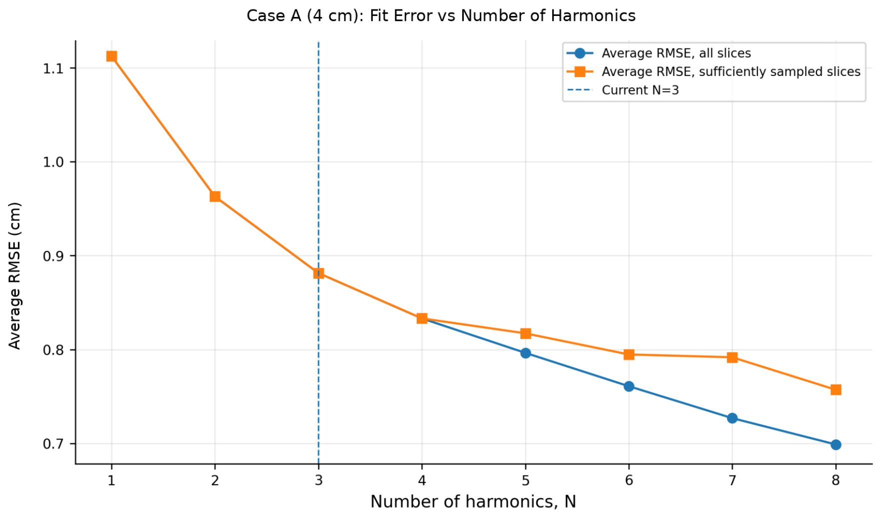

Figure 11. Case A (4 cm): average reconstruction error versus harmonic order. Error decreases as additional Fourier terms are retained; $N = 3$ is used as the common cross-case comparison order rather than as a universal optimum.

3.4. Case B: 5 cm Harmonic Content and Reconstruction Error

Case B contains 144 time slices and 2966 digitized points and was recomputed using the same $N = 3$ basis for comparison with Cases A and C. The harmonic amplitudes in Figure 12 show substantial time variation in all three retained components. These features indicate changing spatial structure in the fitted geometry; they do not establish a one-to-one physical modal decomposition.

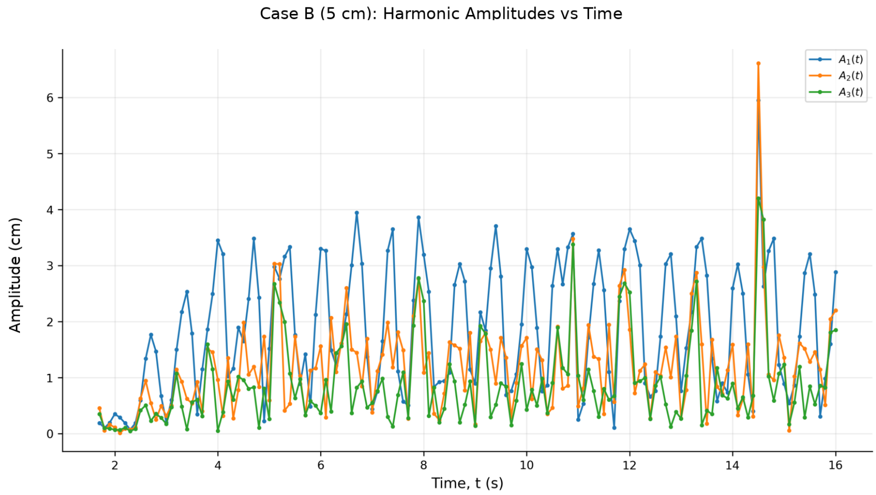

Figure 12. Case B (5 cm): amplitudes of the first three spatial Fourier reconstruction components versus time.

The common $N = 3$ fit gives a mean RMSE of 1.419 cm and a maximum RMSE of 5.962 cm, corresponding to a mean NRMSE of 28.4%. The time-resolved RMSE (Figure 13) contains larger excursions than the two analyzed 4 cm cases. The error continues to decrease as the harmonic order is increased (Figure 14), showing that a three-harmonic truncation leaves appreciable higher-order spatial content in this dataset. The time-resolved RMSE therefore provides the primary record of the larger transient fitting errors in this case.

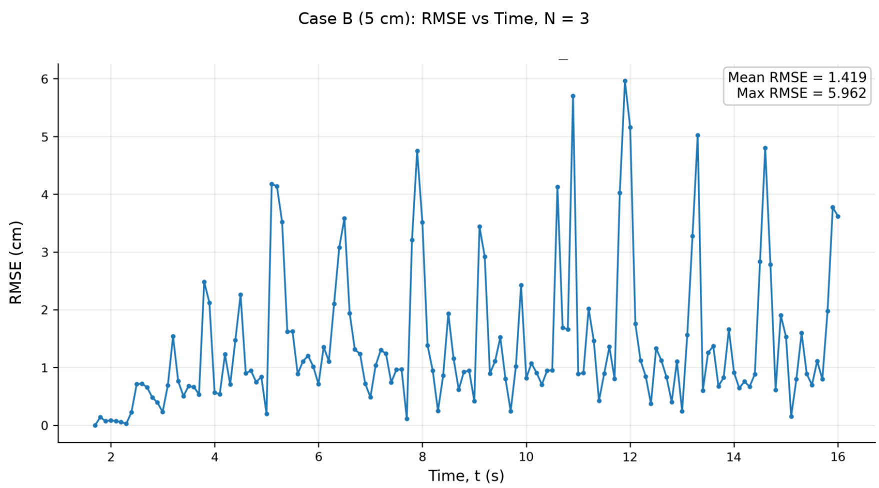

Figure 13. Case B (5 cm): RMSE versus time for the common $N = 3$ reconstruction. Mean RMSE is 1.419 cm and maximum RMSE is 5.962 cm.

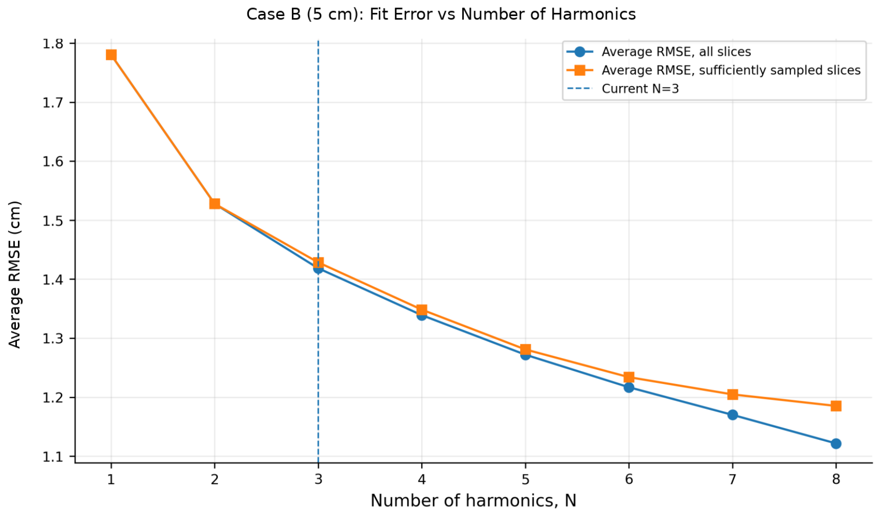

Figure 14. Case B (5 cm): average reconstruction error versus harmonic order. The continuing decrease with increasing N indicates spatial detail that is not fully represented by the common $N = 3$ basis.

3.5. Cross-Case Interpretation

Under the common $N = 3$ reconstruction, the mean RMSE values are 0.8815 cm, 1.419 cm, and 0.5022 cm for Cases A, B, and C, respectively. Normalization by water depth preserves the same qualitative ordering: 22.0%, 28.4%, and 12.6%. Thus, among these three selected records, Case B is the least completely represented by the common low-order basis.

This observation should not be converted into a general claim that 5 cm water depth causes larger reconstruction error. The three datasets are separate experimental records, the excitation kinematics were not fully recorded, the image-acquisition uncertainty was not independently quantified, and only one analyzed dataset is available at 5 cm. The data support a case-level comparison of reconstruction performance, not a statistically general depth effect.

4. Discussion

4.1. Practical Contribution of the Workflow

This study demonstrates a practical route from laboratory wave video to a compact time-dependent mathematical representation. Unlike point measurements, the image-derived coordinates preserve the surface shape over the observed span. Once the coefficients are fitted, the Python applications can evaluate and animate the reconstructed surface as a function of space and time; the final FourierN3 implementation can also interpolate coefficient histories and render a 3D x–t–y reconstructed surface. These operations extend the analysis beyond isolated static fits while remaining conditioned on the measured coefficient histories. They are therefore interpreted as dynamic reduced-order reconstruction rather than as independent physical simulation.

Recent image-based work has pursued automated segmentation, stereo reconstruction, machine learning, and direct image-to-pressure inference [14–17]. The present workflow is intentionally simpler: a calibrated manual extraction is coupled to a transparent low-order reconstruction and residual analysis. This simplicity is useful when the objective is to preserve traceability from each visible point to the final fitted profile. It also makes the limitations easy to identify: manual digitization is labor intensive, and its repeatability should be quantified in future experiments.

The unconventional use of a CNC machining center is a practical experimental feature. It provides a rigid programmable platform capable of repeatable table motion, although the reported runs were not instrumented as a calibrated shaker with synchronized kinematic measurements. The contribution is therefore the experimental use of the platform within the complete image-to-Fourier workflow, not a claim that the present dataset provides a fully characterized excitation transfer function.

4.2. Geometric Interpretation of the Fourier Components

The coefficient histories are most defensibly interpreted in terms of surface geometry. The offset $c_0(t)$ follows the mean vertical position of the fitted profile. The (c_1, c_2) pair gives the broadest periodic spatial component permitted by the chosen basis, and higher pairs represent progressively shorter spatial scales. A growth in A_2 or A_3 therefore indicates that the measured surface shape requires more curvature or shorter-scale structure for its reconstruction.

This geometric interpretation resolves the apparent inconsistency between Equations (2) and (4). The former belongs to physical linear sloshing theory; the latter is a generic periodic basis fitted to data. A quantitative mapping from the fitted coefficients to physical sloshing eigenmodes would require a boundary-condition-consistent modal model and an independently characterized forcing history. Such a mapping is not claimed here.

4.3. Harmonic Order and Under-Fitting

A nested Fourier model will generally show decreasing in-sample error as N is increased. Therefore, the observed reduction in RMSE alone cannot prove that a specific N is statistically optimal. The purpose of $N = 3$ in the present study is comparability and compactness. The Case C comparison demonstrates that $N = 4$ lowers mean RMSE by about 11.8%, and the Case B sensitivity curve shows continued improvement at orders above three. Those results are evidence that a fixed three-harmonic model can under-fit some frames or datasets.

A future automated workflow should choose N using out-of-sample cross-validation or a penalized criterion such as AIC or BIC, with care taken to define independent validation units because neighboring points within a single frame and neighboring frames within a run are correlated. For the current dataset, it is more transparent to present $N = 3$ as a common low-order benchmark and show the observed order sensitivity directly.

4.4. Uncertainty, Robustness, and Statistical Scope

A principal uncertainty limitation is that the original campaign was not designed as a formal metrology study. The image was calibrated in physical coordinates and viewed approximately straight on, but complete camera metadata and a repeated operator study were not retained. Accordingly, no numerical pixel-level or inter-operator confidence interval is assigned retrospectively.

The revised NRMSE provides a meaningful physical-scale benchmark for reconstruction performance. It shows, for example, that a mean RMSE of 0.8815 cm corresponds to approximately 22% of a 4 cm nominal depth. These values are not sufficiently small to characterize every fit as highly accurate; the error curves instead show intervals of both close agreement and substantial mismatch. The residual and profile plots are therefore essential complements to the mean value.

Formal significance testing of the difference between the 4 cm and 5 cm cases would also be inappropriate if each time slice were treated as an independent replicate. Time slices within a run share the same experimental realization and are serially related. With three selected datasets, including only one analyzed 5 cm dataset, the present study is not statistically powered to establish a general causal depth effect. The results are therefore reported descriptively at the dataset level.

4.5. Theoretical Frequency Reference and Interpretation of Case B

Linear theory predicts first-mode reference frequencies of approximately 0.687 Hz for the 4 cm condition and 0.763 Hz for the 5 cm condition in the 0.45 m tank. These values provide theoretical context only because the realized experimental forcing frequency was not independently measured. The larger fitting error observed in Case B therefore cannot be attributed to a verified difference in resonance proximity.

Several non-exclusive explanations remain possible: the actual back-and-forth excitation history may have differed among runs; the 5 cm surface may have contained spatial structure requiring more Fourier terms; reflections and optical visibility may have differed; and manual digitization uncertainty may have varied. The revised manuscript therefore states only that Case B was less completely represented by the common $N = 3$ basis, not that the 5 cm depth itself caused the larger error.

4.6. Limitations and Sources of Error

The principal limitations are as follows. First, the retained controller record documents the programmed CNC displacement range and an approximately 39.8 mm peak-to-peak commanded stroke, but a synchronized independent measurement of the realized $x(t)$ trajectory, acceleration, reversal timing, and forcing frequency was not acquired. The programmed trajectory and nominal feed information therefore do not establish a measured excitation frequency or resonance ratio. Second, the free surface was manually digitized. Reflections, transparency, blur, meniscus effects, calibration choices, and operator point placement can alter the extracted coordinates. Third, a formal repeated-digitization/inter-operator study was not part of the original campaign, so digitization uncertainty cannot be propagated quantitatively into confidence intervals for the Fourier coefficients. Fourth, complete camera metadata were not preserved in the analysis record, although the raw videos remain retained by the authors. Fifth, only three of eleven documented runs were selected for detailed analysis because those records provided the clearest usable free-surface data for consistent digitization; consequently, the findings should not be generalized to all water depths or excitation conditions. Finally, the Python framework provides dynamic and interpolated reconstructions of the fitted wave surface, but those outputs remain conditioned on experimentally derived coefficient histories and therefore do not constitute independent CFD or potential-flow validation.

4.7. Future Work

Future experiments should record the realized CNC table displacement $x(t)$ synchronously from the controller, encoder, or an independent displacement sensor so that the commanded trajectory can be compared with measured stroke, period, velocity, acceleration, and forcing spectrum. This would allow the measured forcing frequency to be compared directly with the theoretical reference frequencies in Table 1.

Image acquisition should be documented with camera model, lens, resolution, frame rate, exposure, viewing distance, and calibration geometry. A representative set of frames should be digitized repeatedly by the same operator and by multiple operators to estimate repeatability and reproducibility. Automated free-surface segmentation, including methods similar to recent AI-based approaches [14], could then be benchmarked against the manually digitized reference profiles.

For model selection, cross-validation or a penalized criterion should be used to choose N rather than imposing a fixed order when the objective is optimal prediction. Finally, a new experimental campaign with fully characterized sinusoidal or programmed excitation should be compared with linear potential-flow predictions and a two-dimensional

CFD/free-surface benchmark. That comparison would provide the independent physics-based validation that is outside the scope of the present retained dataset.

5. Conclusions

This study presents an image-based Fourier reconstruction and analysis workflow for free-surface motion in a CNC-excited rectangular reservoir. The Python software evaluates the experimentally derived Fourier representation in time and space through animated profile reconstruction and, in the final implementation, linearly interpolated coefficient histories and a 3D space–time reconstructed surface. These outputs are dynamic reduced-order reconstructions of the fitted experimental data; they are not independent physical simulations because they do not solve the governing fluid equations or predict the response to a new forcing history.

For the 0.45 m tank, linear theory gives first-mode reference frequencies of approximately 0.687 Hz for the 4 cm condition and 0.763 Hz for the 5 cm condition. The retained CNC controller record documents a programmed peak-to-peak x-axis stroke of approximately 39.8 mm, while the experimental protocol used the estimated natural frequency as a design reference. However, the realized forcing frequency was not independently measured. Consequently, no quantitative resonance ratio or experimentally verified near-resonance condition is claimed. The physical sloshing wave-number relation is also explicitly separated from the generic periodic Fourier basis used for profile fitting.

The workflow was demonstrated on three selected datasets that provided sufficiently clear records for consistent digitization. Under the common, chosen $N = 3$ benchmark, Case A (4 cm) produced a mean RMSE of 0.8815 cm (NRMSE 22.0%), Case B (5 cm) produced 1.419 cm (NRMSE 28.4%), and Case C (4 cm) produced 0.5022 cm (NRMSE 12.6%). For Case C, adding a fourth harmonic reduced the mean RMSE to 0.4427 cm (NRMSE 11.1%), an 11.8% reduction. These RMSE and NRMSE values are fitting errors relative to the manually digitized coordinates and must not be interpreted as estimates of absolute experimental measurement accuracy.

The conclusions are intentionally limited to the three selected records and should not be generalized as a study of water-depth effects. In particular, the larger Case B fitting error cannot be attributed uniquely to water depth because the excitation history and image-measurement uncertainty were not fully characterized. The principal contribution is therefore methodological: a transparent pipeline from CNC-excited wave video to calibrated coordinates, compact Fourier reconstruction, dynamic evaluation of the fitted surface, and quantitative fitting-error diagnostics. Future work should add synchronized excitation kinematics, formal digitization-repeatability analysis, automated surface tracking, objective harmonic-order selection, and independent potential-flow or CFD validation.

Author Contributions: Conceptualization, E.A. and R.A.; methodology, E.A., M.N. and D.B.I.; software, R.A. and O.B.; validation, E.A. and R.A.; formal analysis, E.A. and R.A.; investigation, E.A. and D.B.I.; resources, M.N. and D.B.I.; data curation, R.A. and O.B.; writing—original draft preparation, E.A. and R.A.; writing—review and editing, E.A. and R.A.; visualization, R.A.; supervision, M.N.; project administration, E.A. and M.N.; funding acquisition, M.N. All authors have read and agreed to the published version of the manuscript.

Funding: This research was supported by the Ministry of Science, Technological Development and Innovation of Serbia through Grant No. 451-03-34/2026-03/200105. The experimental setup and measurement equipment were also supported through the strategic bilateral research project conducted from 2018 to 2021 between the Republic of Serbia and the People's Republic of China, entitled "Joint Research on the Development Technology of Low-Head Run-of-the-River Hydropower," in cooperation with the University of Hangzhou. Additional support was provided by the Ministry of Higher Education and Scientific Research of Libya.

Institutional Review Board Statement: Not applicable.

Informed Consent Statement: Not applicable.

Data Availability Statement: The digitized wave-profile datasets, Fourier coefficient files, retained raw experimental videos, and available analysis software/outputs are available from the corresponding author upon reasonable request.

Acknowledgments: The results presented in the paper are part of the results of the research supported by the Ministry of Science, Technological Development and Innovation of Serbia through the Grant number 451-03-34/2026-03/200105 as of 5 February 2026. The authors also gratefully acknowledge the support provided through the Serbia–China bilateral research project and the cooperation of the University of Hangzhou.

Conflicts of Interest: The authors declare no conflicts of interest.

References

1. Faltinsen, O.M.; Timokha, A.N. *Sloshing*; Cambridge University Press: Cambridge, UK, 2009.
2. Ibrahim, R.A. *Liquid Sloshing Dynamics: Theory and Applications*; Cambridge University Press: Cambridge, UK, 2005.
3. Akyildiz, H.; Ünal, E. Experimental investigation of pressure distribution on a rectangular tank due to liquid sloshing. *Ocean Eng.* **2005**, *32*, 1503–1516. [CrossRef]
4. Celebi, M.S.; Akyildiz, H. Nonlinear modeling of liquid sloshing in a moving rectangular tank. *Ocean Eng.* **2002**, *29*, 1527–1553. [CrossRef]
5. Akyildiz, H.; Ünal, N.E. Sloshing in a three-dimensional rectangular tank: Numerical simulation and experimental validation. *Ocean Eng.* **2006**, *33*, 2135–2149. [CrossRef]
6. Yu, L.; Xue, M.-A.; Zhu, A. Numerical investigation of sloshing in rectangular tank with permeable baffle. *J. Mar. Sci. Eng.* **2020**, *8*, 671. [CrossRef]
7. Faltinsen, O.M.; Rognebakke, O.F.; Lukovsky, I.A.; Timokha, A.N. Multidimensional modal analysis of nonlinear sloshing in a rectangular tank with finite water depth. *J. Fluid Mech.* **2000**, *407*, 201–234. [CrossRef]
8. Bäuerlein, B.; Avila, K. Phase lag predicts nonlinear response maxima in liquid-sloshing experiments. *J. Fluid Mech.* **2021**, *925*, A22. [CrossRef]
9. Ren, Y.; Xue, M.-A.; Lin, P. Experimental study of sloshing characteristics in a rectangular tank with elastic baffles. *J. Fluids Struct.* **2023**, *122*, 103984. [CrossRef]
10. Liu, K.; Li, X.; Peng, P.; Zhou, Z.; Gao, Z. Experimental study on the sloshing of a rectangular tank under pitch excitations. *Water* **2024**, *16*, 1551. [CrossRef]
11. Filo, G.; Lempa, P.; Wisowski, K. Review of deterministic and AI-based methods for fluid motion modelling and sloshing analysis. *Energies* **2025**, *18*, 1263. [CrossRef]
12. Tosun, U.; Aghazadeh, R.; Sert, C.; Özer, M.B. Tracking free surface and estimating sloshing force using image processing. *Exp. Therm. Fluid Sci.* **2017**, *88*, 423–433. [CrossRef]
13. Liu, Y.; Dai, J.; Zhang, C. Real-time construction of sloshing-induced hydrodynamic field based on an intelligent image processing technique integrated with artificial damping model. *Ocean Eng.* **2021**, *219*, 108382. [CrossRef]
14. Wei, Z.; Zhai, G.; Wang, Z.; Wang, W.; Ji, S. An artificial intelligence segmentation method for recognizing the free surface in a sloshing tank. *Ocean Eng.* **2021**, *220*, 108488. [CrossRef]
15. Luo, X.; Kareem, A.; Yu, L.; Yoo, S. A machine learning-based characterization framework for parametric representation of liquid sloshing. *Results Eng.* **2023**, *18*, 101148. [CrossRef]
16. Savio, L.; Ahani, A.; Greco, M.; Abrahamsen, B.C. Profilometry: A non-intrusive active stereo-vision technique for wave-profile measurements in large hydrodynamic laboratories. *Exp. Fluids* **2024**, *65*, 137. [CrossRef]
17. Kim, K.J.; Kim, D. Prediction of sloshing pressure using image-based deep learning. *Ocean Eng.* **2024**, *303*, 117718. [CrossRef]
18. Faltinsen, O.M. A numerical nonlinear method of sloshing in tanks with two-dimensional flow. *J. Ship Res.* **1978**, *22*, 193–202. [CrossRef]
19. Liu, D.; Lin, P. A numerical study of three-dimensional liquid sloshing in tanks. *J. Comput. Phys.* **2008**, *227*, 3921–3939. [CrossRef]
20. Zhang, H.; Sun, B. Numerical simulation of sloshing in 2D rectangular tanks based on the prediction of free surface. *Math. Probl. Eng.* **2014**, *2014*, 395107. [CrossRef]
21. Rohatgi, A. WebPlotDigitizer. Available online: https://automeris.io (accessed on 5 June 2026).

22. Haas Automation. VF-3—40-Taper Mill—Vertical Mills. Available online: https://www.haascnc.com/machines/vertical-mills/vf-series/models/medium/vf-3.html (accessed on 5 June 2026).
23. Haas Automation. VF-3SS—40-Taper Mill—Super Speed. Available online: https://www.haascnc.com/machines/vertical-mills/vf-series/models/medium/vf-3ss.html (accessed on 5 June 2026).